Construction and Building Materials 384 (2023) 131467

Contents lists available at ScienceDirect

Construction and Building Materials

journal homepage: www.elsevier.com/locate/conbuildmat

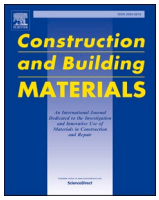

Treatment of fractured concrete via microbially induced carbonate precipitation: From micro-scale characteristics to macro-scale behaviour

Ronald Turner, Gloria M. Castro, James Minto, Grainne El Mountassir, Rebecca J. Lunn *

Department of Civil and Environmental Engineering, University of Strathclyde, United Kingdom

ARTICLE INFO

Keywords:
MICP
Concrete repair
Biomineralization
X-CT
SEM-EDS

ABSTRACT

The development of techniques for concrete repair will reduce environmental impacts associated with concrete usage by extending the lifespan of existing structures. This study investigates microbially induced carbonate precipitation (MICP) for treating fractured concrete. Our results demonstrate the excellent penetrability of MICP with precipitates well-distributed along core length. Some individual treatment cycles resulted in – one order of magnitude reduction in core permeability. Treatment efficiency is shown to be dependent on fracture network characteristics, i.e. number of fractures, fracture orientation, initial hydraulic aperture. Furthermore, bridging of precipitates across fracture surfaces resulted in a recovery of 26–50% of initial tensile strength.

1. Introduction

Concrete constitutes a large proportion of the built infrastructure, with global cement demand for building construction alone reaching close to 2 Gt in 2020 [19]. Concrete assets are often exposed to harsh environmental conditions including exposure to seawater, freeze-thaw cycles, temperature cycles, and, on nuclear sites, exposure to radiation [18,25,30]. The formation of micro-cracks in concrete is common due to its relatively low tensile strength, imposed loading and environmental conditions [48]. As micro-cracks form, they contribute to increasing concrete permeability, which enhance the ingress of undesirable fluids (e.g., corrosive chemical compounds) contributing to further expansion of cracks and ultimately corrosion of reinforcement, with negative impacts on mechanical performance and durability[25,45,48,53]. Reducing the permeability of degraded concrete is key to minimising further deterioration.

The development of inexpensive, low embodied carbon materials and methods for concrete repair will reduce the environmental impacts associated with concrete usage by extending the lifespan of existing structures [33]. Conventional concrete repair techniques include the use of cement or bitumen for surface patching and injections of cement or synthetic polymers (e.g., epoxy resin) into deeper fractures [1,23,26,49]. The application of these traditional repair methodologies, however, can be limited by: (1) particle size and high viscosities, resulting in poor penetration into small aperture cracks, e.g. ultrafine cement viscosities range between 15.4 and 21.5 cP (ULTRAFINE SD™); (2) shrinkage of cements during curing, which may leave pathways for fluid flow; (3) delamination due to the contrast in material properties between concrete and repair materials, e.g. epoxy resins have a different thermal expansion coefficient to concrete and are sensitive to humidity and alkaline environments, which can result in blistering and delamination [34,40]; (4) poor long-term performance of chemical repair techniques [2,13]; and (5) associated negative hazards of repair materials to the environment and human health [48].

Calcium carbonate biomineralisation, and in particular microbially induced carbonate precipitation (MICP) has been investigated for a range of engineering applications including ground improvement [10,51,8], bio-bricks production [28], surface protection of concrete and stone [22,27], crack repair in concrete [29,38,54], production of self-healing concrete [20,47], among other applications [7,36]. MICP has a number of characteristics which makes it a promising novel alternative for concrete repair: (1) the low viscosity of fluids used for MICP treatment (about 1.5 cP, [44] and small bacteria particle size (~2 μm in length, ~0.5micron in diameter) which enables micro-fractures to be penetrated [3], (2) the ability to reduce fracture permeability due to calcium carbonate precipitation [31,46], (3) the similarity of chemical and physical properties between calcium carbonate precipitates and typical binding cement, e.g. both have high calcium content and bulk densities ranging from 1 to 1.4 g/cm^3 [56] ensuring excellent adhesion to surfaces [31,46], (4) MICP treatment can result in strength recovery [21], and (5) potential low application costs of approximately £2.5/m^3 concrete [39].

* Corresponding author.
E-mail address: rebecca.lunn@strath.ac.uk (R.J. Lunn).

https://doi.org/10.1016/j.conbuildmat.2023.131467
Received 1 March 2023; Received in revised form 12 April 2023; Accepted 15 April 2023
Available online 27 April 2023
0950-0618/© 2023 The Authors. Published by Elsevier Ltd. This is an open access article under the CC BY license (http://creativecommons.org/licenses/by/4.0/).

Table 1
Concrete cores properties before MICP treatment.

Core ID	Permeability	Initial Tensile Strength	Mass	First Treatment Flow rate	Initial Average Velocity	Post-Treatment Analysis
	[m^2]	[MPa]	[g]	[ml/min]	[cm/s]	
$C1_L$	$2.35{\cdot}10^{-13}$	3.86	167.05	1	0.99	Tensile strength & SEM
$C2_L$	$8.85{\cdot}10^{-15}$	1.87	171.93	0.25	0.90	SEM
$C3_L$	$4.46{\cdot}10^{-15}$	2.60	162.32	0.4	0.90	Tensile strength
$C4_{LC}$	$7.98\ x10^{-15}$	1.93	172.46	0.3	0.98	None- Control
$C5_{AS}$	$4.27{\cdot}10^{-14}$	–	164.84	0.5	0.95	SEM
$C6_{AS}$	$5.85{\cdot}10^{-14}$	–	173.70	0.5	0.90	SEM
$C7_{ASC}$	–	–	–	–	–	SEM- Control

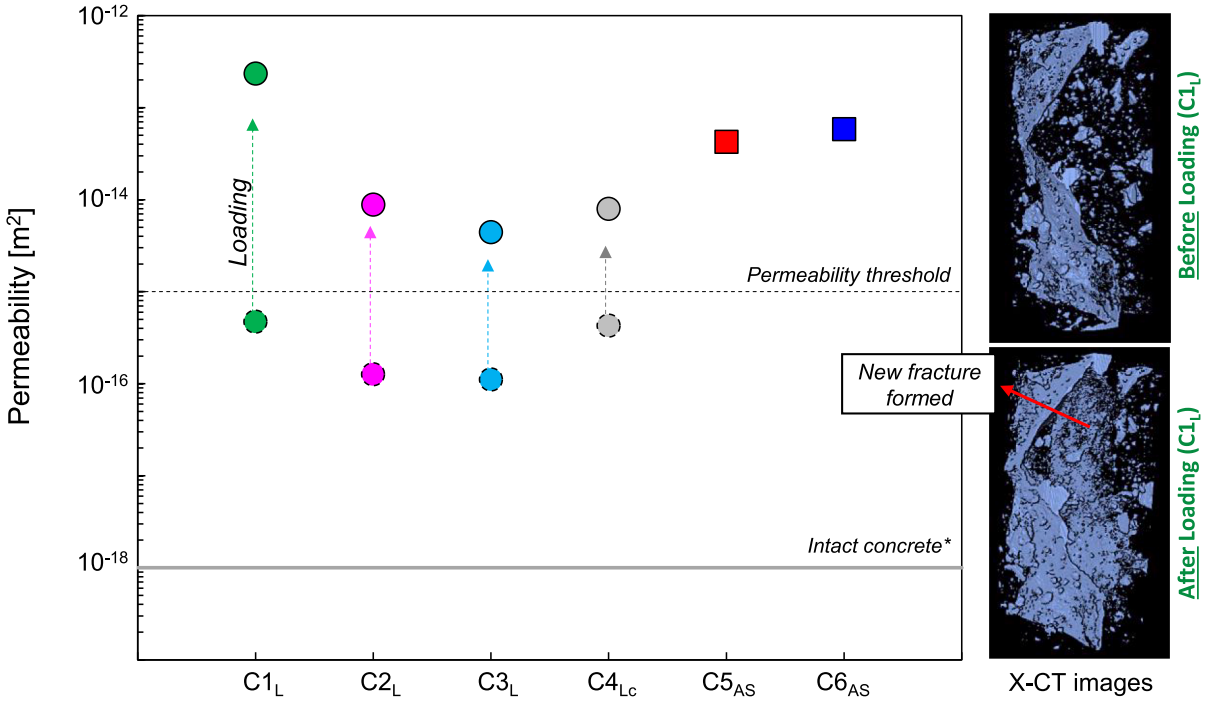

Fig. 1. Concrete specimens preparation. Concrete cores $C1_L$, $C2_L$, $C3_L$ and $C4_{LC}$ displayed an initial permeability value lower than the permeability threshold chosen in this study. These specimens were loaded under Brazilian test conditions. Consequently, concrete permeability increased by the activation of pre-existing fractures and the creation of new fissures as can be seen on the X-CT images (*typical intact concrete permeability value from [43].

Previous studies have relied on pouring/dripping/spraying treatment solutions onto concrete blocks or immersing concrete blocks fully in treatment solutions [14,27,48,53]. These approaches are not practical for in situ application, particularly for application to vertical surfaces of existing structures. Furthermore, studies treating natural/induced fractures and artificially planar fractures in concrete have mainly evaluated crack repair on the basis of visual assessment of the repair at the surface or very close to surface [20,41,48,50] alongside determination of bulk mechanical or hydraulic properties. Limited studies have investigated calcium carbonate distribution into fractures after injected treatments, exceptions to this have included visualisation of carbonate precipitates formed in artificial polycarbonate, granite and cement fractures [15,24,55]. In the aforementioned studies, the fractures treated via MICP were all single, smooth planar fractures.

This study provides a comprehensive experimental and analytical investigation of MICP treatment of 3D fracture networks in degraded concrete. The aims of this paper are to:

Evaluate permeability reduction with progressive cycles of MICP treatment.
Evaluate the potential of MICP to contribute to tensile strength recovery.
Assess the distribution of calcium carbonate precipitated in 3D fracture networks within degraded concrete.
Determine the influence of fracture network characteristics on MICP treatment efficiency.

2. Underlying concepts

2.1. Microbially induced carbonate precipitation (MICP)

In this study, the biomineralisation process investigated is microbially induced carbonate precipitation via urea hydrolysis (MICP). This process relies upon the urease enzyme produced by a bacterium (*Sporosarcina pasteurii*), to catalyse the breakdown of urea to produce ammonia and carbonic acid. Ammonium ions are formed when ammonia dissolves in water, with an associated production of hydroxide ions resulting in a pH increase. As pH increases, carbonic acid is converted to bicarbonate ions and subsequently carbonate ions. In the presence of calcium ions in a high pH environment, the precipitation of calcium carbonate is promoted [16,17,32].

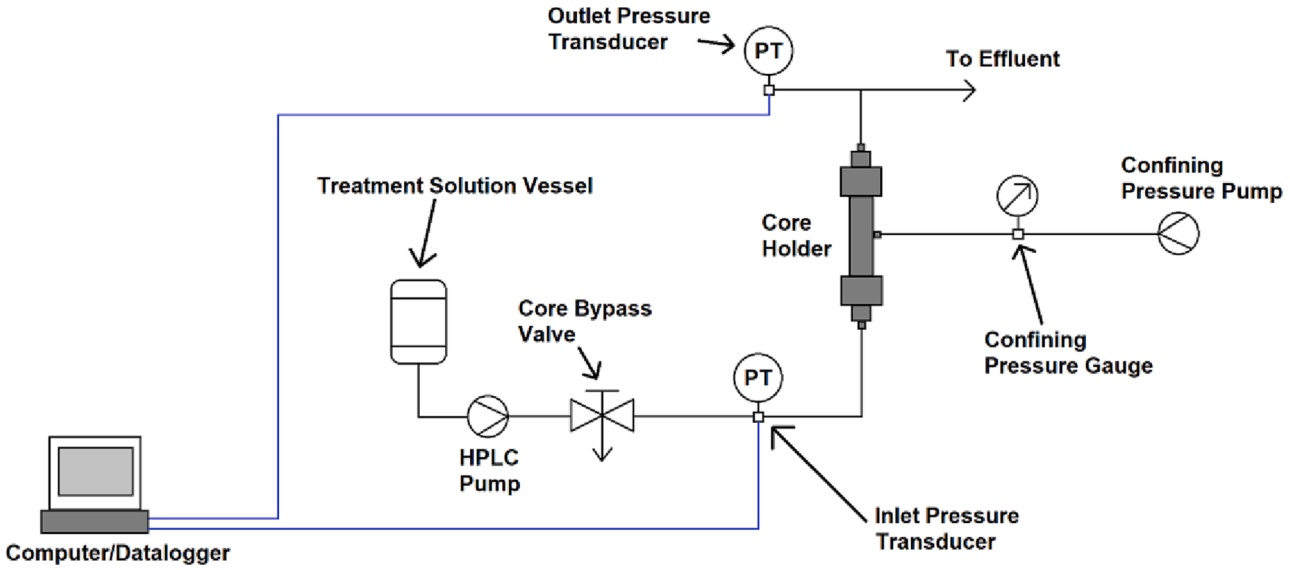

Fig. 2. Experimental Setup: Schematic. Black lines indicate fluid lines, blue lines indicate data lines.

Table 2
Treatment protocol for a single cycle.

Treatment Stage	Treatment Solution	Protocol
1	Water	Measure permeability
2	Bacterial suspension	Inject 5 ml, followed with 15 min static period
3	Water	Inject 5 ml
4	Cementing solution	Inject 5 ml, followed by 60 min static period
5	Cementing solution	Inject 0.5 ml, followed by 600 min static period

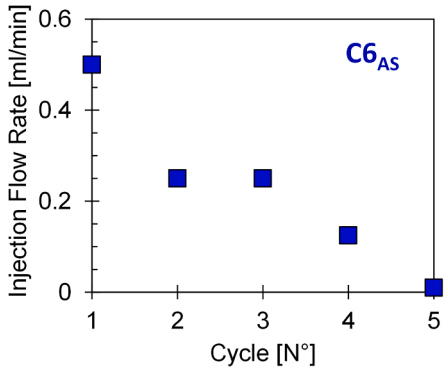

Fig. 3. MICP treatment injection strategy. Example of flow rate evolution in specimen $C6_{AS}$ to maintain an estimated average velocity below 1 cm/s.

2.2. Flow through a porous medium

Darcy's law describes fluid flow through a porous medium driven by a pressure difference Δp [Pa], where the flow rate q [m^3/s] is highly dependent on the medium permeability k [m^2] and the dynamic viscosity of the pore fluid μ [Pa·s] as follows [12]:

$$q = \frac{kA}{\mu}\frac{\Delta p}{L} \quad [1]$$

where A [m^2] is the cross-sectional area and L [m] is the flow path length.

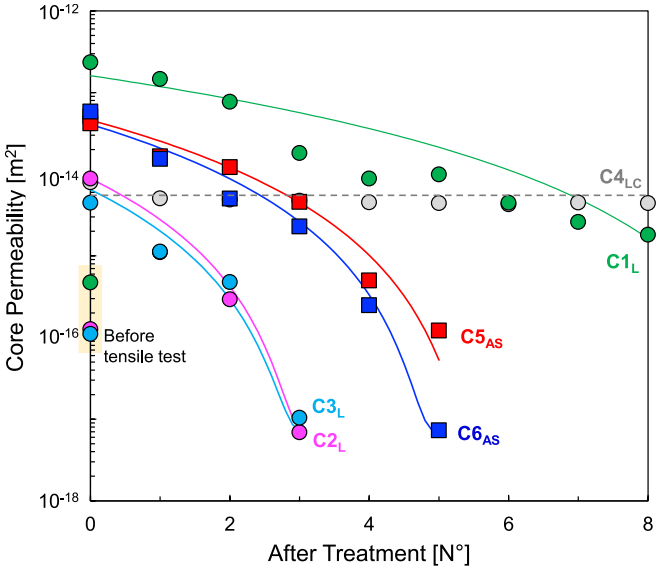

Fig. 4. Core permeability evolution after each MICP treatment cycle. Circles display specimens that were loaded prior to MICP treatment and squares show results for concrete cores subjected to MICP treatments as sampled (i.e. not preloaded). Lines display analytical model results detailed in the discussion section.

2.2.1. Flow through naturally fractured concrete

Fluid flow through a fractured concrete volume involves flow through a heterogeneous medium. On one hand, typical matrix permeability k_m values are in the range of 10^{-20} to 10^{-18} m^2 orders of magnitude depending on the water to cement ratios and concrete overall quality [43,52]. In contrast, fracture permeability k_f is proportional to its aperture a, ($k_f = a^2/12$), following the cubic law [42], resulting in permeability values in the order of 10^{-8} m^2 for a fracture aperture a = 0.5 mm. In fact, in this study, estimations of treatment fluid velocities use measurements of permeability to calculate hydraulic apertures a, assuming that just the fracture contributes to fluid flow. Combining equation [1] with the hydraulic aperture definition above, we calculated the average fluid velocity $\overline{V}$, assuming a steady state flow between infinite parallel flat plates, with:

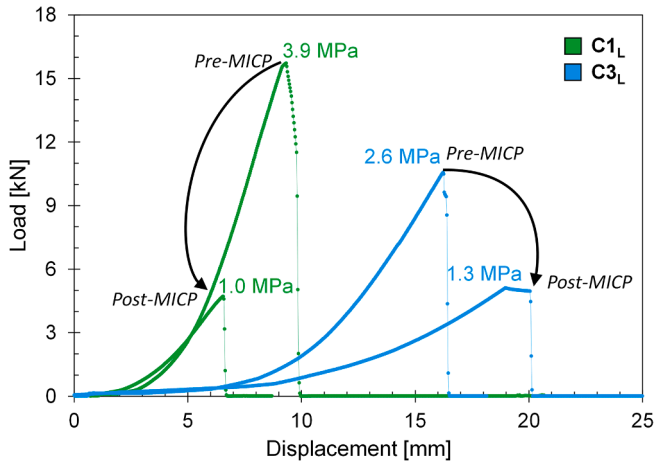

Fig. 5. Brazilian test: Tensile strength. Both cores $C1_L$ and $C3_L$ show an important strength recovery after MICP treatment, varying from a 26 to 50% of the initial strength.

$$\overline{V} = \frac{\Delta p \bullet a^2}{12\mu \bullet L} \quad [2]$$

The effective permeability k_{eq} represents the combined permeability of the matrix and fractures in a fractured concrete medium. Fracture orientation with respect to the direction of fluid flow is critical for effective permeability. For example, in a concrete core where the fracture and matrix are in parallel and aligned with the fluid flow direction, then by mass conservation:

$$q_{total} = q_{matrix} + q_{fracture} \quad [3]$$

$$k_{eq} \bullet i \bullet A_{total} = k_m \bullet i \bullet A_m + k_f \bullet i \bullet A_f \quad [4]$$

where i is the hydraulic gradient. Assuming that the specimen is a cylinder of radius r containing a single parallel smooth fracture, the cross-sectional area of the fracture is defined as $A_f = 2 \bullet r \bullet a$, and the cross-sectional area of the matrix is the remaining cross-section $A_m = \pi r^2 - A_f$. Then, the effective permeability can be expressed as:

$$k_{eq} \bullet (\pi r^2) = k_m \bullet (\pi r^2 - 2 \bullet r \bullet a) + k_f \bullet 2 \bullet r \bullet a \quad [5]$$

$$k_{eq} = k_m \left(1 - \frac{2 \bullet a}{\pi r}\right) + \frac{a^3}{6\pi r} \quad [6]$$

Considering that the fracture thickness a is much smaller than the specimen radius r, then:

$$k_{eq} \approx k_m + \frac{a^3}{6\pi r} \quad [7]$$

3. Materials and methods

3.1. Concrete specimens

The experimental study used degraded concrete blocks that consisted of waste mass and reinforced concrete that was emplaced as part of a coastal protection scheme from an intertidal zone along the Ayrshire coast, Scotland. The concrete blocks were exposed to wetting-drying cycles by seawater due to tidal changes over a period of ~50 years, resulting in salt accumulations of 8 g/kg concrete (estimated from electrical conductivity measurements) and a highly porous concrete matrix.

A total of seven concrete cores of 36 mm diameter by 72 mm length were sampled from the collected concrete blocks. Table 1 displays the initial properties of each specimen. MICP treatment was conducted on cores $C1_L$, $C2_L$, $C3_L$, $C5_{AS}$, $C6_{AS}$. Fig. 1 displays the initial permeability values for each specimen. Cores identified with L subscript were subjected to loading following Brazilian tensile test conditions [5] in order to enhance their initial permeability above the threshold identified in Fig. 1, prior to MICP treatment. The permeability threshold shown in Fig. 1 was set in order to ensure that all cores had a similar initial permeability. Tensile loading increased specimen initial permeability by the activation of pre-existing fractures and creation of new fissures as can be seen in the X-ray Computed Tomography (X-CT) images in Fig. 1. Specimens were wrapped within a heat-shrink tube around each core to facilitate specimen handling after tensile loading, X-CT imaging and mounting in the core holder for treatment. Using a heat-shrink tube provides protection to heavily fractured specimens to minimise loss of aggregates/fragments during sample mounting, core characterization and application of MICP treatment (the tube was removed after the core was treated). Cores identified with subscript AS were treated as-is, i.e. no tensile loading was conducted before treatment. Cores $C4_{LC}$ and $C7_{ASC}$ were control cores. $C4_{LC}$ was treated chemically only (i.e. no bacteria were injected into this core) and $C7_{ASC}$ was imaged as-is via Scanning Electron Microscopy (SEM) with no water injection or MICP treatment applied. Each specimen was weighed before treatment by oven drying the cores at 50 °C to a constant mass (Table 1). Multiple concrete cores from the same source material were treated in this study to understand the repeatability of the efficiency of MICP treatment in realistic fractures.

Brazilian tests were used to evaluate the tensile strength for cores $C1_L$ and $C3_L$ post-MICP treatment, care was taken to ensure the cores were mounted in the same orientation as in the pre-treatment tensile test. Additionally, polished blocks were prepared from cores $C1_L$, $C2_L$, $C5_{AS}$, $C6_{AS}$ for SEM-Energy Dispersive Spectroscopy (SEM-EDS) analyses after MICP treatment and for $C7_{ASC}$ (as-is). Note the polished blocks for Core $C1_L$ were prepared from material recovered after the post-treatment tensile strength test.

3.2. Bacterial suspension

This study used *Sporosarcina pasteurii* (*S. pasteurii*) (DSMZ, DSM-33) as it has been shown to have the highest performance in terms of mass of precipitates formed in comparison to other ureolytically active bacteria [35]. *S. pasteurii* was grown from cryopreserved stock cultures in a solid medium consisting of 5.5 g/L yeast extract (Sigma-Aldrich), 5 g/L sodium chloride (Fisher Scientific), 0.4 g/L D-glucose (Sigma-Aldrich), 0.4 g/L dipotassium phosphate (Sigma-Aldrich), 20 g/L urea (Sigma-Aldrich), and 15 g/L agar (Sigma-Aldrich). Urea was added aseptically after autoclaving all other components of the medium.

A single colony from the solid medium was then transferred into a liquid growth medium with the same composition as the solid medium listed above, but without the addition of agar to avoid solidification. The liquid medium was then incubated overnight at 30 °C. After incubation, the culture was centrifuged at 6000 rpm for 7 min to obtain pellets of bacterial cells that were subsequently re-suspended in mains tap water to achieve an optical density (OD_{600}) at a fixed wavelength of 600 nm using a spectrophotometer (Thermo Scientific UV–VIS) equal to 1.0. This formed the bacterial suspension for injection into the cores. The bacterial suspension was prepared immediately prior to starting a new MICP treatment cycle.

3.3. Treatment strategy

The concrete cores were immersed in water, followed by the application of vacuum to achieve water saturated conditions. The cores were then mounted in a core holder and a confining pressure of 2 MPa applied (Fig. 2) to ensure by-pass flow did not occur around the outer boundary of the core. A HPLC pump was used to inject fluids at a controlled flow rate through the core and pressure transducers at the inlet and outlet ports were used to measure the pressure differential along the core. Taking a conservative approach and assuming flow only occurs within

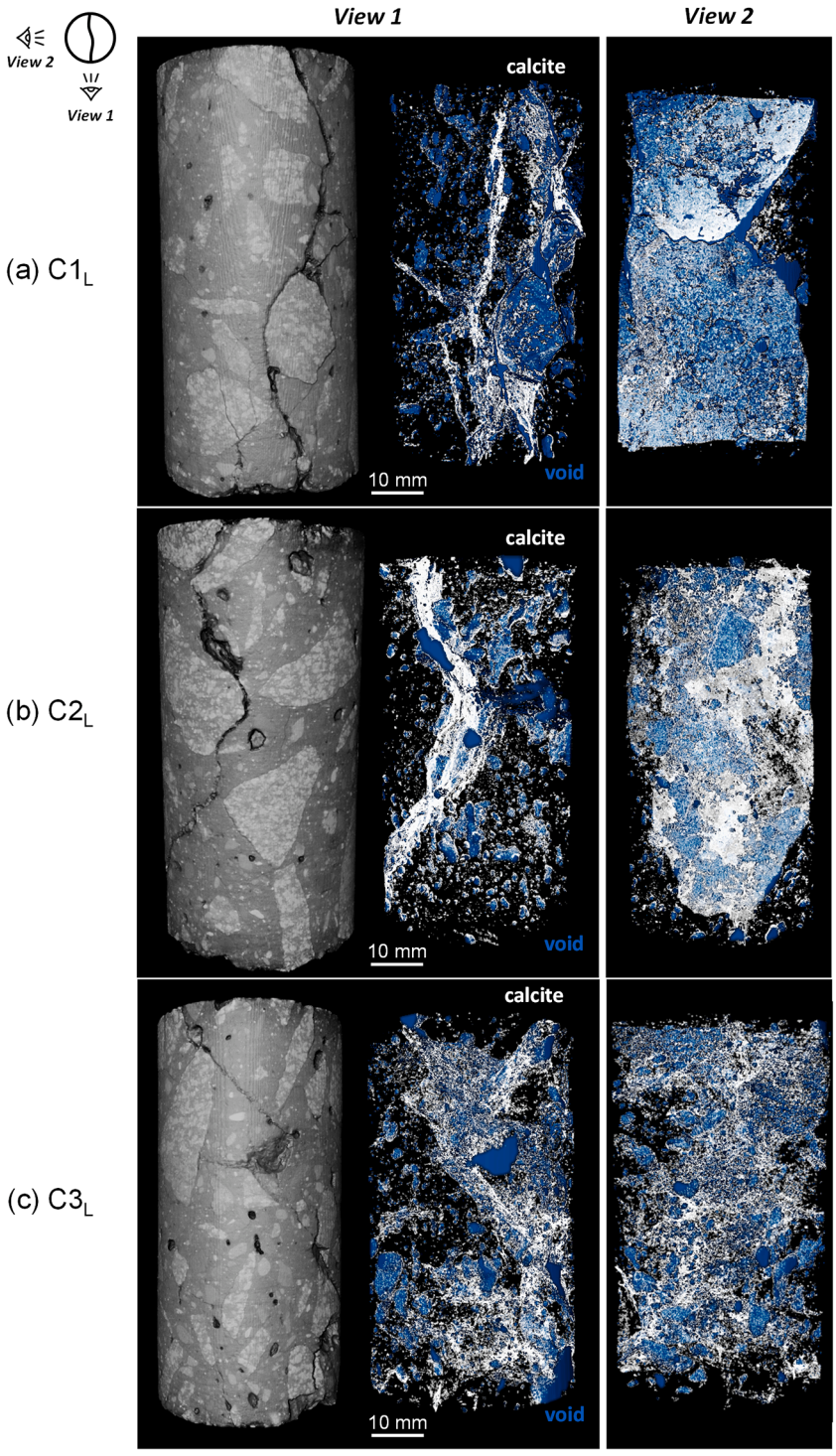

Fig. 6. Calcite precipitation distribution along concrete cores. Cartoon shows top of concrete core and the directions of the two view perspectives with respect to the fracture surface. Figures (a) to (e) display X-CT images of the concrete cores where white volumes show precipitated calcite derived from pre and post treatment scanning, and blue shows the core's remaining void volume after MICP treatment.

the fracture, the initial fracture hydraulic aperture (pre-treatment) was evaluated on the basis of a permeability measurement and calculated using the cubic law [Equations 1 and 2, where$\overline{V} = q/(a \bullet r)$]. Using the determined initial hydraulic aperture, initial injection flow rates were selected such that an average velocity of 1 cm/s was not exceeded within the fracture (Table 1). This velocity threshold was selected to ensure that any deposited/attached bacteria were not sheared off fracture surfaces [15].

Table 2 summarises the stages of a single MICP treatment cycle. After the permeability measurement, 5 ml of bacterial suspension was injected followed by a 15-minute static period to allow the bacteria to attach to solid surfaces. Then, 5 ml of water was injected to separate the bacterial suspension and cementing solution in order to prevent calcite precipitation occurring within the pump and tubing lines. Afterwards, 5 ml of

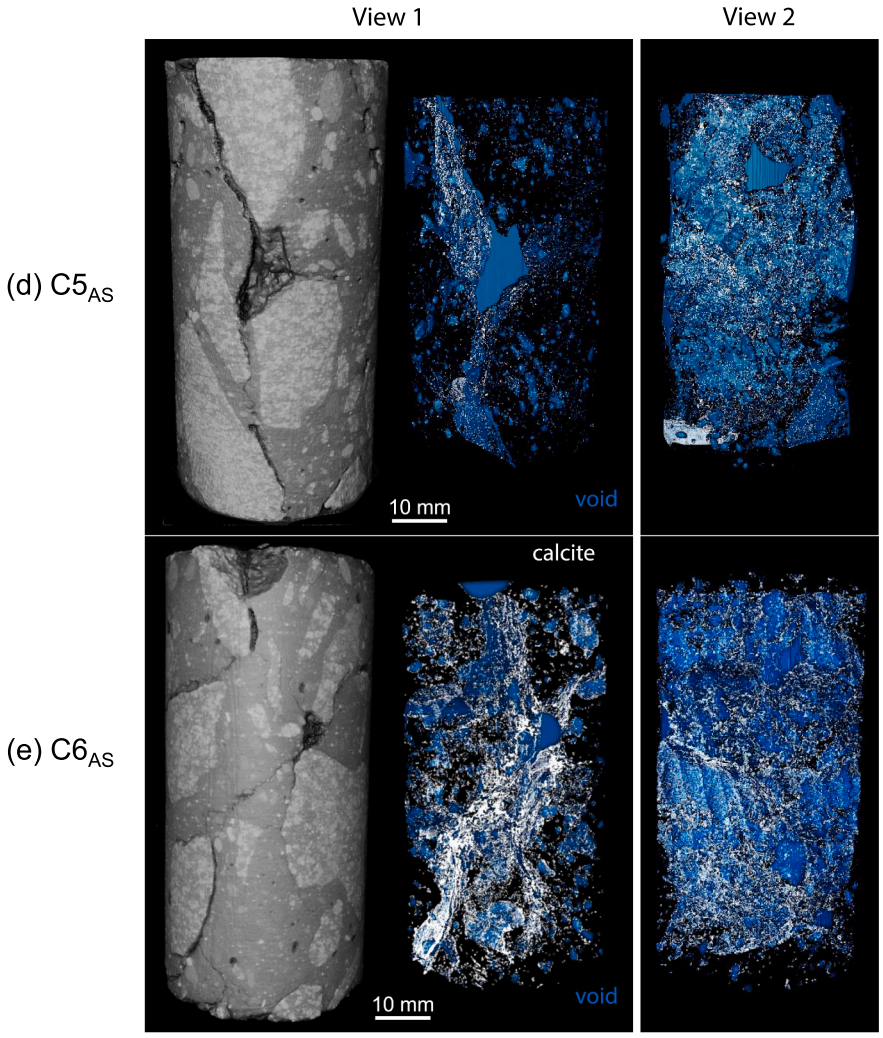

Fig. 6. (*continued*).

the cementing solution was injected. The cementing solution was composed of 1 M calcium chloride (Sigma-Aldrich) and 1 M urea (Sigma-Aldrich). This was followed by a 60 min static period. Finally, 0.5 ml of cementing solution was injected to provide a 'refresh' prior to 600 min of static period.

Each concrete core was subjected to repeated treatment cycles. As the cross-sectional area of the fracture reduced with progressive calcium carbonate precipitation, the injection flow rates used for MICP treatment were progressively stepped down to ensure that the threshold average velocity of 1 cm/s within the fracture was not exceeded (e.g., $C6_{AS}$ treatment flow rates in Fig. 3). MICP treatment was stopped once two-orders of magnitude of permeability reduction was achieved or when an injection pressure of 80 kPa was exceeded due to pressure limitations in the experimental setup. Each treatment cycle for specimen $C4_{LC}$ (control core) excluded the bacterial suspension injection stage (Treatment Stage 2).

3.4. Precipitates advanced characterization

3.4.1. X-ray computed tomography (X-CT)

Tomographic imaging provides visualization of the pore space before and after treatment. In this study, a Nikon XT H 225 LC X-ray Computed Tomography system was used. Images of the concrete cores were taken under saturated conditions using an energy of 120 kV, current of 125 μA, 1.415 s of exposure time and a voxel size of 45 μm. Reconstruction of 2D projections to 3D volumes included corrections for beam hardening.

Avizo software was used to analyse X-CT volumes. The generalized workflow included: (1) registration of pre- and post-treatment stacks, (2) applying an anisotropic diffusion filter to emphasize the void-to-solid contrast, (3) thresholding of void volumes on each case, and (4) subtraction of pre-treatment images from the post-treatment images. This data processing allowed visualization of the precipitated calcite within void spaces.

3.4.2. Scanning electron microscope SEM-EDS

SEM-EDS analyses of treated specimens enables the visualisation of micro-scale characteristics which may be linked to core-scale behaviour. This study used a S-3700 SEM (Hitachi) machine fitted with an 80 mm X-Max detector (Oxford Instruments) for EDS analysis. Specimens were prepared by impregnating the concrete cores with epoxy resin, followed by preparation of polished blocks (31 mm diameter and 14 mm thickness). A gold layer coating of ~15 nm thick was applied to each polished block prior to SEM analysis.

4. Results

4.1. Permeability

Fig. 4 presents the core permeability measured after each MICP treatment calculated using Equation 1. Every MICP treatment cycle

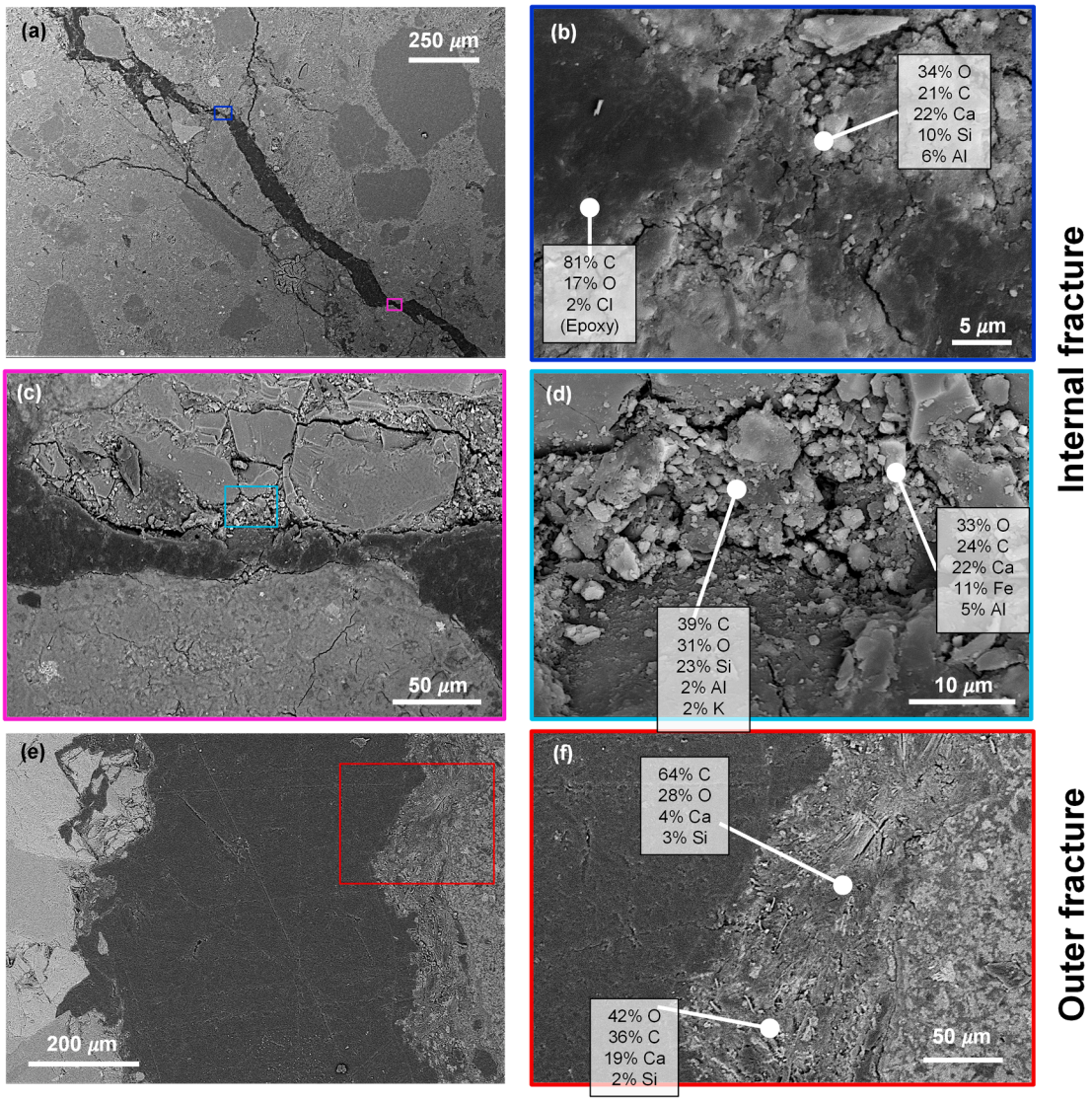

Fig. 7. SEM-EDS imaging of core $C1_L$. This specimen was failed by tensile test and reconstructed for SEM imaging. The internal fracture shows narrower channels in comparison with the outer fracture affecting fluid flow and consequently precipitates localization.

significantly reduced concrete permeability in all five treated cores ($C1_L$, $C2_L$, $C3_L$, $C5_{AS}$, and $C6_{AS}$), with some individual cycles reducing permeability by approximately one order of magnitude, e.g., treatment 1 in cores $C2_L$ and $C3_L$ (shown as pink and blue circles). As expected, the control core $C4_{LC}$ (shown as grey circles), which followed the same treatment cycles but excluded the bacterial suspension injection step, did not display any significant reduction in permeability after eight cycles.

4.2. Tensile strength

Pre- and post-treatment Brazilian tensile test results display a tensile strength recovery between 26 and 50% of the initial strength (Fig. 5). Both specimens tested after treatment failed within the MICP treated fractures, resulting in similar tensile strengths achieved in both cores (1 MPa vs. 1.3 MPa).

4.3. Microstructural analysis

4.3.1. X-CT visualization

The processed X-CT images of each MICP treated core shown in Fig. 6 enable visualization of the precipitates distribution (shown in white) and the remaining void spaces after MICP treatment (shown in in blue). In general, cores $C2_L$, $C3_L$, $C5_{AS}$, $C6_{AS}$ each comprised a single principal fracture aligned with the flow direction (i.e., aligned in the vertical direction of the core). In contrast, X-CT images showed that core $C1_L$ comprised two parallel unconnected principal fractures. The pre-loaded specimens ($C1_L$, $C2_L$, $C3_L$ and $C4_L$) show fracture planes that are similarly tortuous to the as-sampled specimens ($C5_{AS}$, $C6_{AS}$), with fracture planes wrapping around aggregates in specimens in both categories. It can be seen from Fig. 6 that calcite precipitates are highly localized in the dominant fracture with some precipitates located in apparently disconnected pore spaces. See 3D visualization in the supplementary data videos for further details.

4.3.2. SEM-EDS characterization

Figs. 7-9 present SEM images of the MICP treated specimens. EDS analysis was used to determine elemental composition at different locations indicated by position of white spots. In general, the remaining open fractures after MICP treatment are shown in dark grey which indicates the presence of the epoxy resin which impregnated the remaining open void spaces and fractures during preparation of the polished block sections.

Fig. 7 presents the SEM images for Core $C1_L$. Polished blocks were

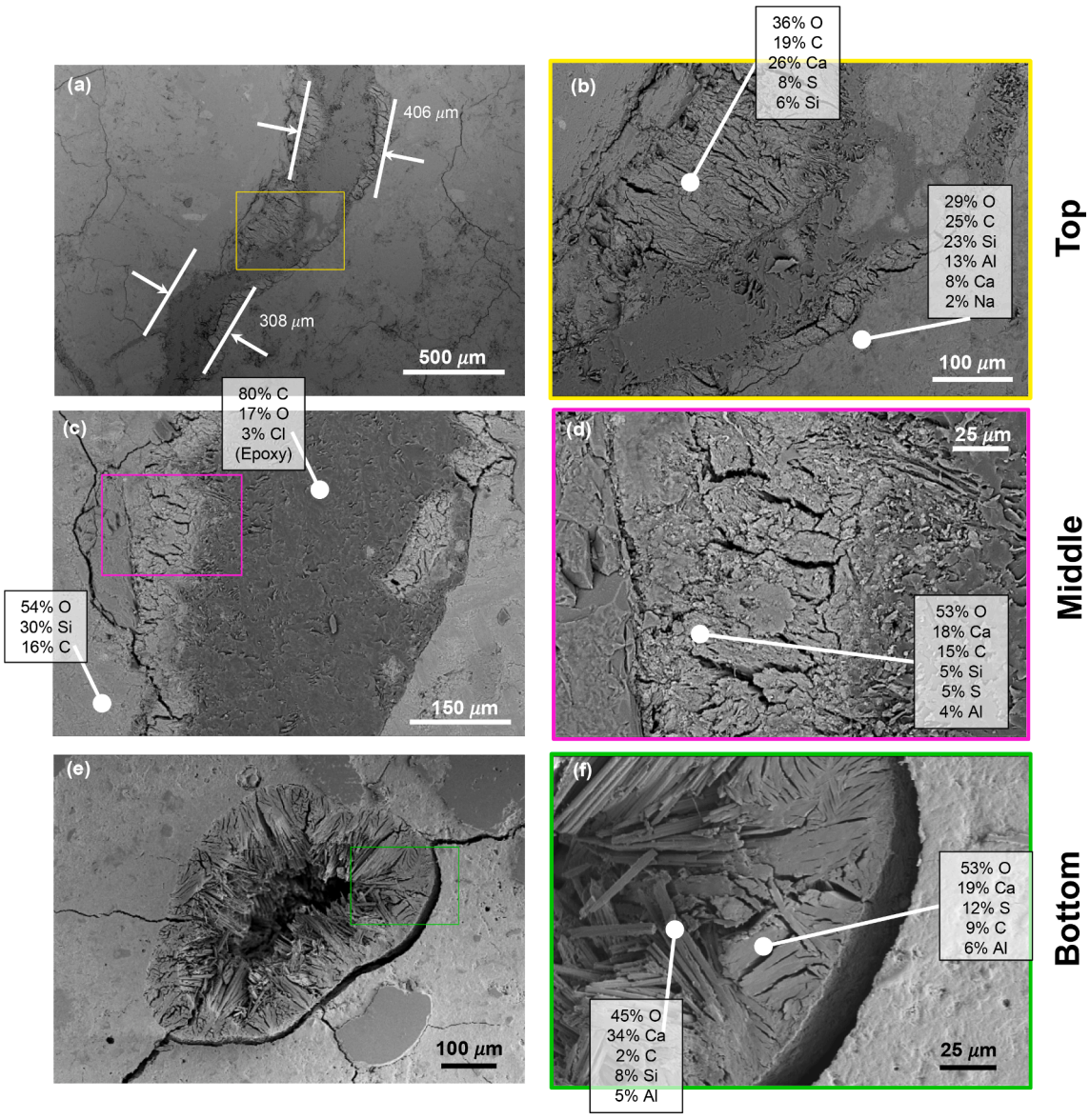

Fig. 8. SEM-EDS imaging of core $C2_L$. SEM images display precipitates localization in the fracture's curvature edges, consequent to slower flow rates.

prepared from the failed specimen so as to enable imaging of both principal fractures present in Core $C1_L$, referred to here as the internal fracture and the outer fracture (note: specimen failed through the outer fracture during tensile test). Evidence of mineralisation was observed along both the internal and outer fractures. EDS analysis indicates interactions with the cement matrix with the calcium carbonate precipitates rich in silicon, aluminium, and iron (all components of cement). The internal fracture in $C1_L$ is considerably narrower than the outer fracture, with mineralisation focussed on constrictions, whereas for the wider outer fracture mineralisation was evident along the fracture length (and appeared to have a greater thickness).

Fig. 8 presents the SEM images for Core $C2_L$. In these images it is evident that calcium carbonate precipitation is controlled by velocity distribution, with thicker zones of precipitates observed on curvatures of bends within the fractures probably due to changes in velocity due to aperture variations at these locations, see Fig. 8a and b. Likewise, the distribution of precipitates within the middle section of the core displayed localization at low velocity areas (Fig. 8c and d). Mineralisation was also observed to occur within voids (Fig. 8e).

Fig. 9 presents the SEM images of Core $C5_{AS}$. Mineralisation is evident both within voids and within the fracture. The presence of sulphur and magnesium in this treated as-sampled specimen suggests interaction with existing salt precipitates already coating surfaces, during MICP treatment, with potential co-precipitation of gypsum ($CaSO_4$) and dolomite ($CaMg(CO_3)_2$) occurring. Sections were prepared at various distances from the inlet, mineral precipitation was observed along the full length of the cores and did not appear to be dependent on distance from the inlet. The tortuous nature of the fracture in $C5_{As}$ (Fig. 9) is similar to the fractures created by pre-loading in $C1_L$ and $C2_L$ (Figs. 7 and 8) with the tortuous flow paths (and local velocity distributions) governing the localization of precipitates.

In Fig. 9c it is clear that MICP induced precipitation can contribute to the formation of bridges between fracture surfaces. This explains the mechanism for tensile strength recovery demonstrated in section 4.2 above. Furthermore, MICP precipitates do not display a sharp interface with the original concrete, suggesting the potential for excellent adhesion to the concrete surface.

Fig. 10 shows the SEM images of the untreated control specimen $C7_{AS}$ that was sampled as-is and was not subjected to any treatment fluids. It is evident that the fracture surfaces are much cleaner than for the MICP-treated core $C5_{AS}$, although there are still some salt layers present which are rich in sulphur, magnesium and sodium, typical of

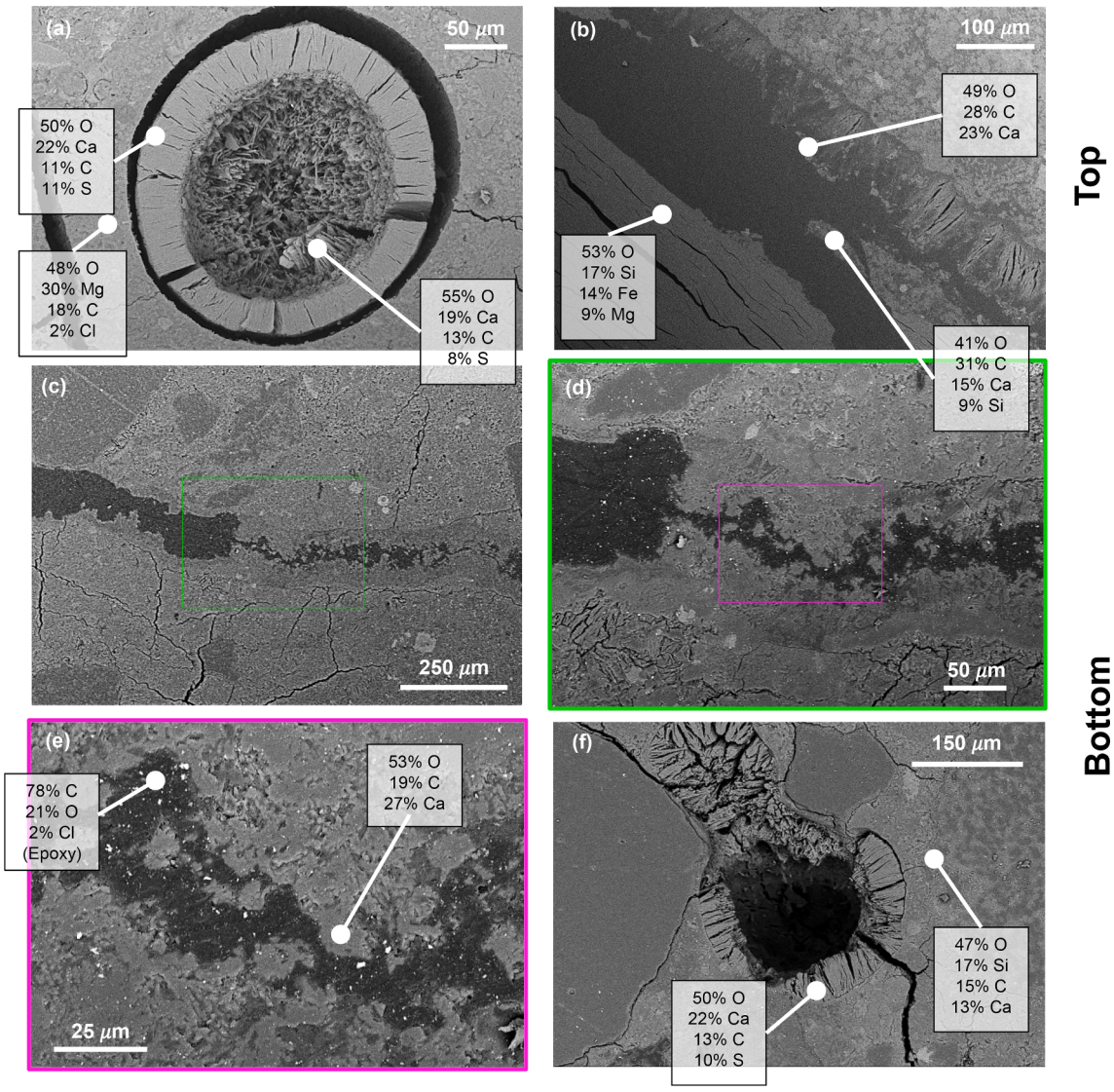

Fig. 9. SEM-EDS imaging of core $C5_{AS}$. MICP treatment driven precipitates are clear in both fractures and visually isolated voids from X-CT imaging. There is no clear precipitates localization with respect to inlet–outlet ports (bottom vs. top).

precipitates formed in seawater.

5. Discussion

5.1. Calcite precipitation in naturally fractured concrete

This study has shown that MICP can be used for permeability reduction of naturally fractured concrete. Furthermore, using degraded concrete specimens, this research builds upon previous analyses where MICP treatment has been used to treat single, planar and smooth artificial fractures. In this study, the fracture networks in the concrete cores that were tested as-sampled were similar to the fracture networks created in the specimens that were loaded prior to MICP treatment. In particular, high tortuosity of the fracture planes, rough fracture surfaces and changes in fracture width along fluid paths were properties that were evident and similar in each of the five MICP-treated cores (Figs. 7-10). These properties promote bacteria entrapment and, consequently, calcite precipitation. For example, fracture tortuosity, rough surfaces and changes in fracture width all result in areas with higher retention times and preferential flow paths, producing regions of localized precipitation (e.g., see narrow path in Fig. 7a and c and tortuous path and changes in fracture width in Fig. 9a, Fig. 10b and c).

In contrast, however, we do not observe localization of precipitates with respect to distance from the injection point on SEM-EDS images (Fig. 8 and Fig. 9). Fig. 11 shows the volume occupied by MICP-driven precipitates at a given depth in each core, where every single datapoint represents the volume measured on a X-CT slice of 45 μm thickness perpendicular to the flow direction. Likewise, measured precipitates regions along MICP treated cores from X-CT images do not show a preferential mineralization towards either the inlet or outlet ports (Fig. 11).

Additionally, SEM images highlight the localization of precipitates within cross-sections perpendicular to the flow direction in the principal fracture, also evident from X-CT analyses. Using the Separate Objects function (output type: connected objects) from Avizo, we isolated the hydraulically disconnected pore volumes from the main fracture and measured the volume occupied by precipitates on the resulting images in core $C1_L$ (Fig. 12). The reduction in precipitates volume, when hydraulically disconnected volumes are not considered, is ~5% which confirms the high localization of MICP-driven precipitates within the principal fractures. In particular, precipitates show an overall homogenous distribution along the axis parallel to fluid injection, with higher volumes of precipitates in regions where the initial fracture had more volume (e.g. at 48–50 mm from the inlet, where more calcite is

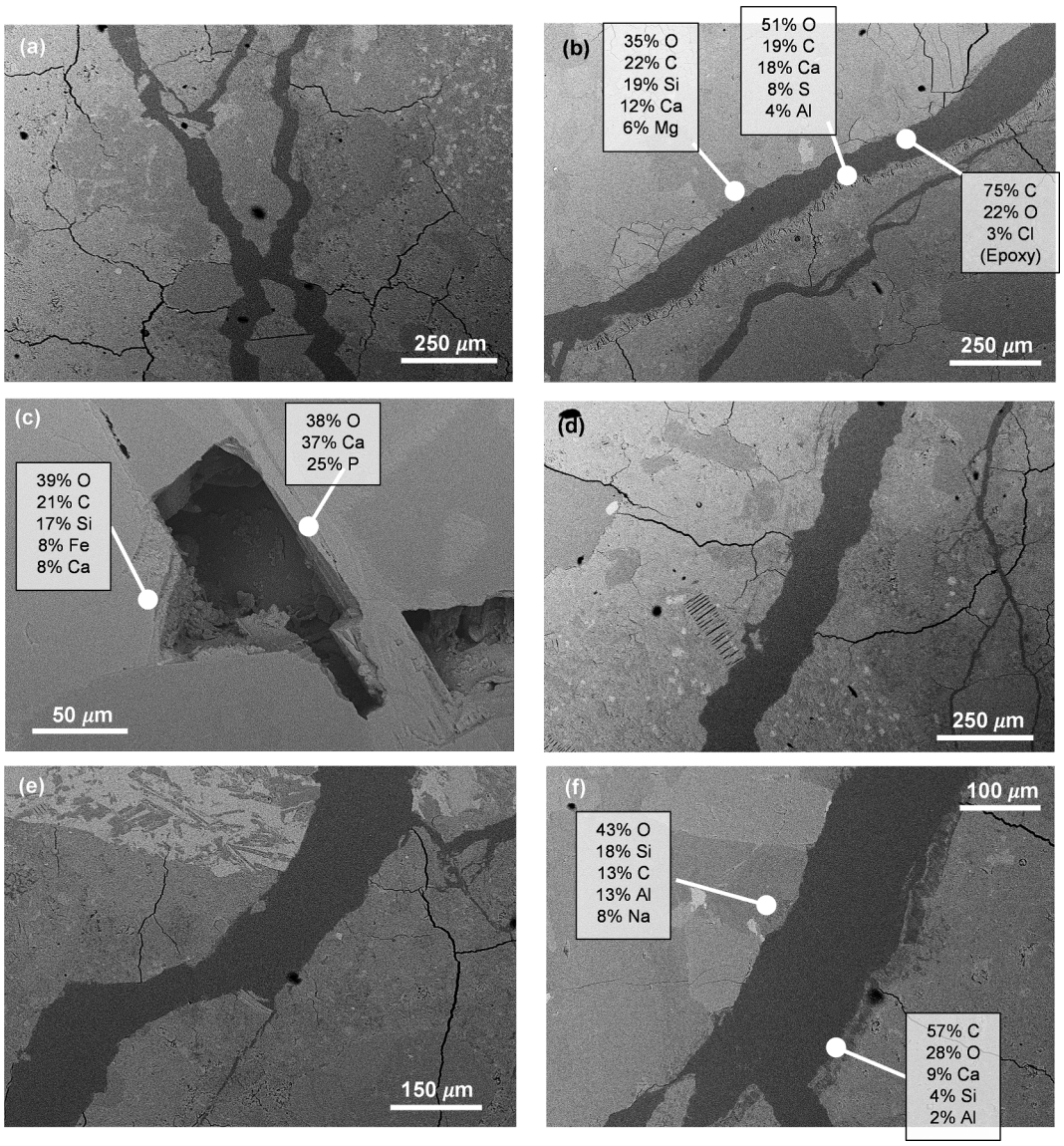

Fig. 10. SEM-EDS imaging of core $C7_{ASC}$. Imaging of this untreated and not loaded core displays significantly cleaner fractures. Nevertheless, some fractures display typical seawater salt precipitates.

precipitated, Fig. 12b, as there is more space to precipitate in, Fig. 12a). These observations suggest that the injection strategy employed resulted in good mixing, preventing clogging near the inlet port.

SEM-EDS analyses confirmed the presence of calcite precipitation in apparently disconnected voids, connected by micro- and nano-pores in the cement matrix below the X-CT scanner resolution (e.g., Fig. 8e and f, Fig. 9a and f). As similar observations were not made for the control sample C7, this demonstrates the excellent penetrability of MICP treatment fluids (due to their low viscosity and small particle size of bacteria).

The concrete material used in this study had been exposed, prior to sampling, to ~50 years of harsh environmental conditions including exposure to seawater. Consequently, MICP-driven precipitation displayed high contents of sulphur, magnesium, aluminium, and iron even in specimens loaded before MICP treatment (i.e. where the fracture surfaces were freshly created). This may result from the dissolution and transport of salts located in pre-existing open fractures and within the concrete matrix. Previous studies conclude that seawater does not significantly influence bacterial production of calcium carbonate when the calcium source is calcium chloride [37]. Nevertheless, the same study showed a reduction of about 35% in tensile strength when a sand specimen was MICP treated in the presence of seawater in comparison with a specimen treated using fresh water. These results are in line with the observations in this study where we measured repair strengths lower than previous works (i.e., 1.3 MPa in this study vs 3–5 MPa in [6]. Similarly, we do not observe the more thermodynamically stable rhombohedral calcite crystals [4,11]. In particular, needle-like crystals (potentially aragonite) were observed to form in disconnected pores which suggests that the pre-existence of cations (derived from cement and seawater precipitates) may be driving co-precipitation of various minerals. Still, MICP-driven precipitates appear to be well adhered to fracture surfaces, i.e. there is not a sharp interface between fracture edges and precipitates. Future work applying MICP treatment to concrete media exposed to seawater may consider pre-treating voids, by water flushing to reduce salt accumulations.

Finally, significant reductions in permeability and substantial tensile strength recovery are a result of the preferential localization of precipitates at fracture contacts and the formation of bridges between fracture surfaces (see Fig. 5 and Fig. 9c). Chen et al. [9] have shown that the size of the calcium carbonate crystals formed is highly dependent on the calcium concentration in the injection cementing solution. In our study we have used a calcium concentration of 1 M, the research by

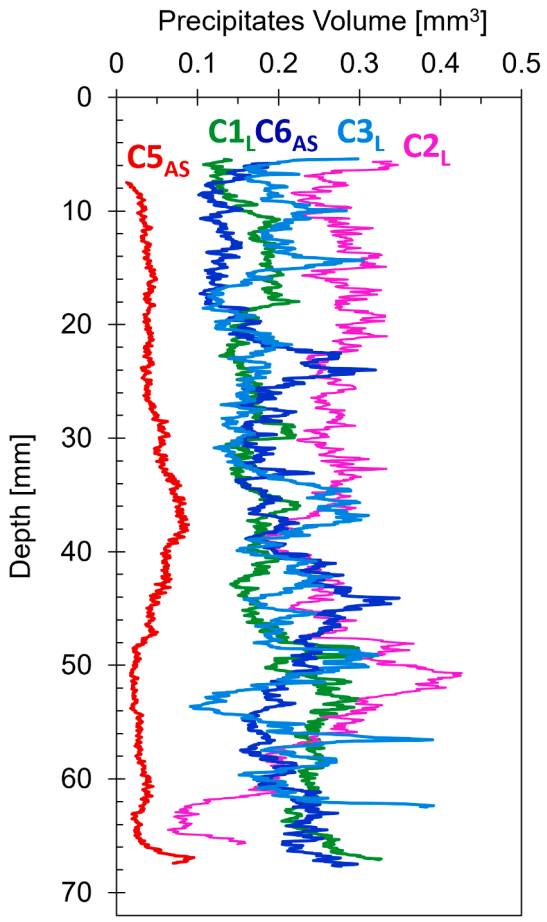

Fig. 11. Precipitates localization in all voids along MICP treated cores measured from X-CT slices of 45 μm thickness.

Chen et al., suggests that it may be possible to bridge fractures more quickly using a lower calcium concentration (0.4–0.8 M), by forming large agglomerated crystals, with diameters up to 200 μm. The recovery of tensile strength in the fractured cores in this study and the fact that failure occurred within the precipitates (rather than at the interface between fracture and precipitates) indicates excellent adhesion of the precipitates to the fractures surfaces (both cement matrix and aggregates).

5.2. MICP-driven permeability reduction

Fracture orientation, frequency, and aperture control permeability in fractured media. In this study, all cores (treated after loading and as-sampled) had one dominant fracture extending from the base to the top of each core, with the exception of core $C1_L$ that had two unconnected principal fractures (see X-CT images in Fig. 6 and Fig. 13). MICP treatment fluid flow is predominantly controlled by the main connected volume path. Consequently, most of the precipitates would be expected to be localized in the main fracture of each core.

Permeability measurements after each treatment cycle indicate that the injection strategy used required a different number of cycles to achieve a given permeability reduction in each core (Fig. 4). Nevertheless, hydraulic aperture reduction, calculated from measured permeability after each cycle [using Eqn 2 where $\overline{V} = q/(a \bullet r)$], shows a consistent reduction of ~5 μm/cycle in all cores with a single controlling fracture (Fig. 13, cores $C2_L$, $C3_L$, $C5_{AS}$, $C6_{AS}$). In Fig. 13 Core $C1_L$ permeability reduction is controlled by two treatment periods with different slopes, which is consistent with the presence of two principal fractures, as observed in the X-CT images. The variation in hydraulic aperture reduction rates reflects differences in the aperture of the two fractures; as different volumes of injected fluids are transported through each fracture (Fig. 7).

Assuming that each MICP treatment cycle reduces only the fracture aperture (i.e. matrix permeability is not affected) we can model permeability reduction as a function of the MICP cycles using Eqn 7. Continuous lines in Fig. 4 show the model results for each concrete core tested in this study. Table 3 shows model parameter values, where initial fracture aperture estimates are derived from initial permeability measurements, matrix permeability values are consistent between all tested specimens, and aperture reduction per MICP cycle reflects measured values (Fig. 13). In concrete core $C1_L$, assuming a single fracture model, the initial fracture hydraulic aperture was calculated to be 50 μm. However, two dominant fractures were observed in the X-CT images for this core (Fig. 6a). Assuming a similar total hydraulic aperture reduction per cycle to those measured in the other specimens (Fig. 13 and Table 3) it is possible to calculate an initial hydraulic aperture for each fracture. Based on this assumption, one fracture, with hydraulic aperture a_1, has an initial aperture of 12.5 μm and the second, more dominant fracture, has a hydraulic aperture a_2 of 37.5 μm.

Evidently, fracture morphology is a controlling factor that defines MICP treatment efficiency. Treated concrete cores in this study come from the same source block and therefore display similar fracture morphology as fracture formation is highly dependent on the density of aggregates, their shape, and grain size; hence resulting in similar MICP treatment efficiencies.

5.3. Injection strategy

The treatment injection strategy used in this study resulted in consistent and efficient hydraulic aperture reduction in all five concrete cores, which displayed micron-scale natural fracture networks. Additionally, localization of precipitates was not observed around the inlet or outlet port but instead the spatial distribution of calcite was driven by fracture morphology. In general, controlling the injection flow rate to limit fracture velocities below 1 cm/s acted to promote bacteria retention within the core, and static periods allowed for an even distribution of calcite precipitation along the core's length. Consequently, repaired specimens displayed significant strength recovery, with similar tensile strength values for both specimens tested post-treatment.

6. Conclusions

Microbially Induced Carbonate Precipitation has emerged as a promising technique for concrete improvement. This study proposes and applies an efficient injection strategy to repair degraded concrete material. For the first-time this study investigated the spatial distribution of calcite precipitation within 3D fracture networks, consisting of non-planar, rough and tortuous fractures. X-CT imaging and SEM-EDS analyses were used to investigate the distribution of carbonate precipitates with permeability measurements and Brazilian tensile strength tests conducted to understand the influence of MICP on macro-scale engineering behaviour. The mains conclusions are:

- The treatment protocol proposed and tested in this study results in good penetrability and well-distributed precipitates along the principal fracture. Some individual treatment cycles reduced core permeability by – one order of magnitude. Additionally, precipitates that localized in isolated voids confirm MICP treatment reagents can also be transported along micro-scale fissures (below the detected limit of X-CT imaging in this study, with a voxel size of 45 μm).
- MICP-driven precipitates localise at fracture contacts and form bridges across fracture surfaces providing significant reductions in permeability and strength recovery.
- It is evident that fracture morphology has a major role in MICP treatment efficiency. Assessments of MICP treatment efficiency

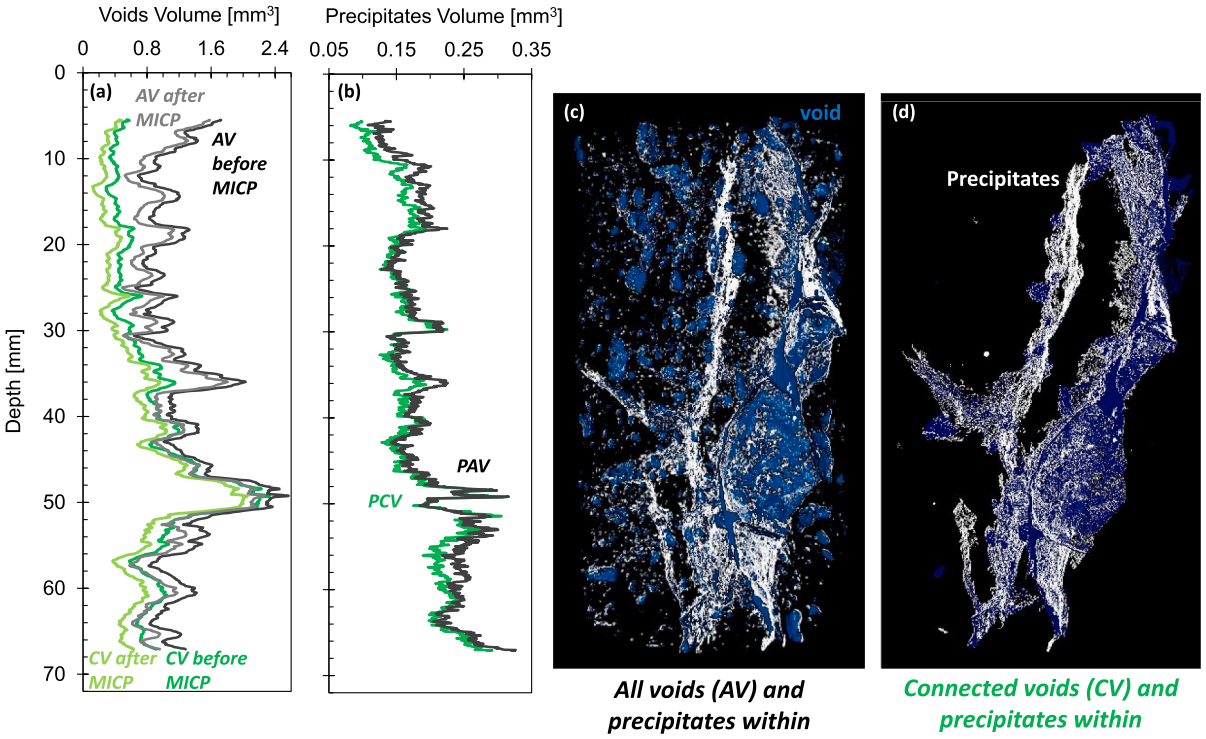

Fig. 12. Precipitates localization along principal fractures: $C1_L$. (a) Variation of the volume of voids with depth before and after MICP treatment considering all the voids (AV) and only the connected voids (CV). (b) Distribution of the volume of precipitates along the core considering precipitation within all voids PAV and only precipitation within connected voids PCV. (c) X-CT image of all the voids in the core and MICP-driven precipitates. (d) X-CT image of the connected voids within the core and the precipitates within. Calculations of volumes in (a) and (b) use 45 μm thick X-CT slices.

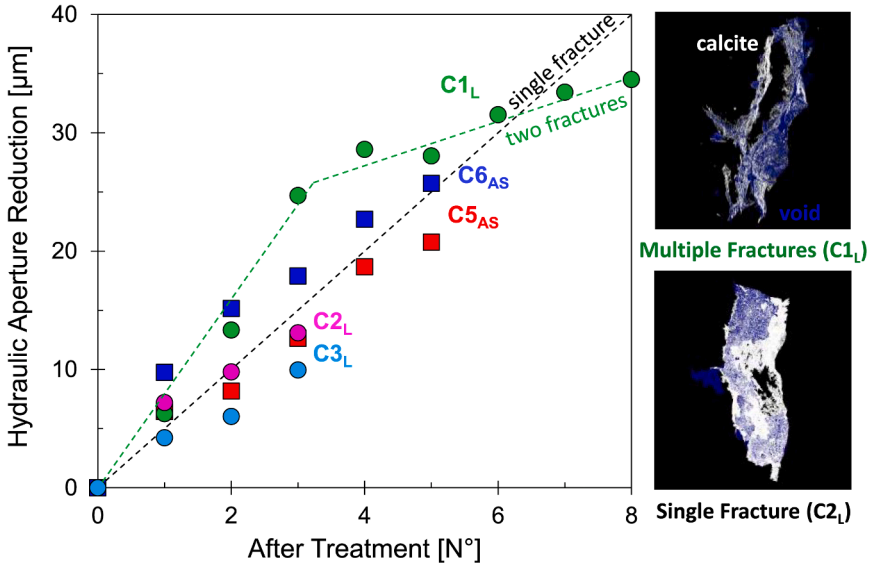

Fig. 13. Hydraulic aperture reduction. X-CT images in the right show the connected void spaced of cores $C1_L$ and $C2_L$.

should consider real fractured concrete (rather than simple smooth, planar models), as tortuosity, roughness, fracture width and orientation are key in permeability evolution.

- The biomineralisation-based concrete repair method described in this study has significant potential to treat damaged concrete in real-world applications. Further work will focus on the translation of this treatment process beyond the laboratory scale and treatment of millimeter-scale fractures.

Declaration of Competing Interest

The authors declare that they have no known competing financial interests or personal relationships that could have appeared to influence the work reported in this paper.

Table 3
Permeability model parameters.

Core	Matrix Permeability k_m [m^2]	Initial Fracture Hydraulic Aperture a [μm]	Hydraulic Aperture Reduction Per Cycle [μm]
$C1_L$	$7 \bullet 10^{-18}$	a_1 = 12.5 & a_2=37.5	4.9*
$C2_L$	$7 \bullet 10^{-18}$	14.4	4.6
$C3_L$	$7 \bullet 10^{-18}$	13	4.2
$C5_{AS}$	$7 \bullet 10^{-18}$	25	4.5
$C6_{AS}$	$7 \bullet 10^{-18}$	24	4.8

* total, where a_1 accounts for 25% of total aperture reduction and a_2 75%.

Data availability

The following materials which support this publication are available for public access: https://doi.org/10.15129/c63675d6-3796-4c1e-9c88-f9f4913e10eb.

Acknowledgements

This research was funded by the Engineering & Physical Sciences Research Council (EPSRC) [EP/R004889/1], the Royal Academy of Engineering [RCSRF1718\5\35] and by the industry partners of the Advanced Nuclear Research Centre at the University of Strathclyde (ANRC-013-01): Babcock, BAM Nuttall Ltd., Bruce Power, EDF Energy. For the purpose of Open Access, the authors have applied a Creative Commons Attribution (CC BY) to any Author Accepted Manuscript (AAM) version arising from this submission. The authors also wish to thank Philip Pearson for his support in collecting the concrete samples and technician Jim Francis for preparing the concrete cores for testing. The authors would like to acknowledge that the microstructural analyses (X-CT and SEM) were carried out in the Advanced Materials Research Laboratory, at the University of Strathclyde.

Appendix A. Supplementary data

Supplementary data to this article can be found online at https://doi.org/10.1016/j.conbuildmat.2023.131467.

References

[1] A.M. Aguirre-Guerrero, R. Mejía de Gutiérrez, in: Eco-Efficient Repair and Rehabilitation of Concrete Infrastructures, Elsevier, 2018, pp. 315–353.
[2] M.J. Al-Kheetan, M.M. Rahman, D.A. Chamberlain, Influence of early water exposure on modified cementitious coating, Construction and Building Materials 141 (2017) 64–71, https://doi.org/10.1016/j.conbuildmat.2017.02.159.
[3] S. Bhaduri, T. Ghosh, C. Montemagno, A. Kumar, Sporosarcina pasteurii can form nanoscale crystals on cell surface, BioRxiv 184184 (2017), https://doi.org/10.1101/184184.
[4] Bragg, W. L. (1924). The structure of aragonite. Proceedings of the Royal Society of London. Series A, Containing Papers of a Mathematical and Physical Character, 105 (729), 16-39.
[5] British Standards Institutes (2009). BS EN 12390-6: 2009, Testing Hardened Concrete. Tensile Splitting Strength of Test Specimens. British Standard Institution, London, UK.
[6] R. Cardoso, E. Arbabzadeh, J.T. de Lima, I. Flores-Colen, M.F.C. Pereira, M. Costa e Silva, S.O.D. Duarte, G.A. Monteiro, The influence of stone joints width and roughness on the efficiency of biocementation sealing, Construction and Building Materials 283 (2021) 122743.
[7] R. Cardoso, R. Pedreira, S. Duarte, G. Monteiro, H. Borges, I. Flores-Colen, Biocementation as rehabilitation technique of porous materials, New Approaches to Building Pathology and Durability (2016) 99–120.
[8] Y.Q. Chen, S.Q. Wang, X.Y. Tong, X. Kang, Crystal transformation and self-assembly theory of microbially induced calcium carbonate precipitation, Applied Microbiology and Biotechnology 106 (9–10) (2022) 3555–3569.
[9] Y. Chen, S. Wang, XinYang Tong, X. Kang, Towards the sustainable fine control of microbially induced calcium carbonate precipitation, Journal of Cleaner Production 377 (2022) 134395.
[10] S.G. Choi, I. Chang, M. Lee, J.H. Lee, J.T. Han, T.H. Kwon, Review on geotechnical engineering properties of sands treated by microbially induced calcium carbonate precipitation (MICP) and biopolymers, Construction and Building Materials 246 (2020), 118415, https://doi.org/10.1016/j.conbuildmat.2020.118415.
[11] Y. Dai, H. Zou, H. Zhu, X. Zhou, Y. Song, Z. Shi, Y. Sheng, Controlled synthesis of calcite/vaterite/aragonite and their applications as red phosphors doped with Eu 3 + ions, CrystEngComm 19 (20) (2017) 2758–2767.
[12] Darcy, H. (1856). Les fontaines publiques de la ville de Dijon: exposition et application des principes à suivre et des formules à employer dans les questions de distribution d'eau... un appendice relatif aux fournitures d'eau de plusieurs villes au filtrage des eaux (Vol. 1). Victor Dalmont, éditeur.
[13] W. De Muynck, N. De Belie, W. Verstraete, Microbial carbonate precipitation in construction materials: a review, Ecological engineering 36 (2) (2010) 118–136.
[14] W. De Muynck, D. Debrouwer, N. De Belie, W. Verstraete, Bacterial carbonate precipitation improves the durability of cementitious materials, Cement and Concrete Research 38 (7) (2008) 1005–1014, https://doi.org/10.1016/j.cemconres.2008.03.005.
[15] G. El Mountassir, R.J. Lunn, H. Moir, E. Maclachlan, R.J. Lunn, H. Moir, E. Maclachlan, Hydrodynamic coupling in microbially mediated fracture mineralization: Formation of self-organized groundwater flow channels, Water Resources Research 50 (1) (2014) 1–16, https://doi.org/10.1002/2013WR013578.
[16] F.G. Ferris, L.G. Stehmeier, United States Patent 5143155, United States Patent, 1992.
[17] F.G. Ferris, L.G. Stehmeier, A. Kantzas, F.M. Mourits, Bacteriogenic mineralplugging, Journal of Canadian Petroleum Technology 35 (8) (1996) 56–61, https://doi.org/10.2118/96-08-06.
[18] D.W. Hobbs, Concrete deterioration: Causes, diagnosis, and minimising risk, International Materials Reviews 46 (3) (2001) 117–144, https://doi.org/10.1179/095066001101528420.
[19] IEA. (2021). Global cement demand for building construction, 2000-2020, and in the Net Zero Scenario, 2025-2030 – Charts – Data & Statistics - IEA. https://www.iea.org/data-and-statistics/charts/global-cement-demand-for-building-construction-2000-2020-and-in-the-net-zero-scenario-2025-2030.
[20] J. Intarasoontron, W. Pungrasmi, P. Nuaklong, P. Jongvivatsakul, S. Likitlersuang, Comparing performances of MICP bacterial vegetative cell and microencapsulated bacterial spore methods on concrete crack healing, Construction and Building Materials 302 (2021) 124227.
[21] P. Jongvivatsakul, K. Janprasit, P. Nuaklong, W. Pungrasmi, S. Likitlersuang, Investigation of the crack healing performance in mortar using microbially induced calcium carbonate precipitation (MICP) method, Construction and Building Materials 212 (2019) 737–744, https://doi.org/10.1016/J.CONBUILDMAT.2019.04.035.
[22] F. Jroundi, M.T. Gonzalez-Muñoz, A. Garcia-Bueno, C. Rodriguez-Navarro, Consolidation of archaeological gypsum plaster by bacterial biomineralization of calcium carbonate, Acta biomaterialia 10 (9) (2014) 3844–3854.
[23] Y. Jung, T.J. Freeman, D.G. Zollinger, Guidelines for Routine Maintenance of Concrete Pavement, In Texas Transportation Institute Vol (2008) FHWA/TX-08.
[24] C.M. Kirkland, D. Norton, O. Firth, J. Eldring, A.B. Cunningham, R. Gerlach, A. J. Phillips, Visualizing MICP with X-ray μ-CT to enhance cement defect sealing, International Journal of Greenhouse Gas Control 86 (2019) 93–100, https://doi.org/10.1016/J.IJGGC.2019.04.019.
[25] W. Kubissa, M.A. Glinicki, M. Dąbrowski, Permeability testing of radiation shielding concrete manufactured at industrial scale, Materials and Structures/Materiaux et Constructions 51 (4) (2018), https://doi.org/10.1617/s11527-018-1213-0.
[26] W. Kurdowski, Cement and concrete chemistry, Cement and Concrete Chemistry 9789400779457 (2014) 1–700, https://doi.org/10.1007/978-94-007-7945-7.
[27] G. Le Metayer-Levrel, S. Castanier, G. Orial, J.F. Loubiere, J.P. Perthuisot, Applications of bacterial carbonatogenesis to the protection and regeneration of limestones in buildings and historic patrimony, Sedimentary geology 126 (1–4) (1999) 25–34.
[28] S. Liu, K. Du, W. Huang, K. Wen, F. Amini, L. Li, Improvement of erosion-resistance of bio-bricks through fiber and multiple MICP treatments, Construction and Building Materials 271 (2021), 121573, https://doi.org/10.1016/j.conbuildmat.2020.121573.
[29] Lu, C. & Li, Z. (2022). Durability assessment of repairing vertical cracks in concrete using microbially induced calcium carbonate precipitation technique.
[30] R.E. Melchers, I.A. Chaves, Service life estimation of concrete infrastructures, in: Eco-Efficient Repair and Rehabilitation of Concrete Infrastructures, Elsevier, 2018, pp. 15–41.
[31] J.M. Minto, E. MacLachlan, G. El Mountassir, R.J. Lunn, Rock fracture grouting with microbially induced carbonate precipitation, Water Resources Research 52 (11) (2016) 8827–8844, https://doi.org/10.1002/2016WR018884.
[32] A.C. Mitchell, K. Dideriksen, L.H. Spangler, A.B. Cunningham, R. Gerlach, Microbially enhanced carbon capture and storage by mineral-trapping and solubility-trapping, Environmental science & technology 44 (13) (2010) 5270–5276.
[33] R. Muigai, Eco-efficient design of concrete repair and rehabilitation, in: Eco-Efficient Repair and Rehabilitation of Concrete Infrastructures, Elsevier, 2018, pp. 591–611.
[34] National Academies of Sciences Engineering and Medicine. (2012). Long-Term Performance of Polymer Concrete for Bridge Decks. The National Academies Press. 10.17226/14623.
[35] P. Nayanthara, A. Dassanayake, K. Nakashima, S. Kawasaki, Microbial induced carbonate precipitation using a native inland bacterium for beach sand stabilization in nearshore areas, Applied Sciences 9 (15) (2019) 3201, https://doi.org/10.3390/app9153201.
[36] V.L. Pacheco, L. Bragagnolo, C. Reginatto, A. Thomé, Microbially Induced Calcite Precipitation (MICP): Review from an Engineering Perspective, Geotechnical and Geological Engineering 40 (5) (2022) 2379–2396.

[37] J. Peng, T. Cao, J. He, D. Dai, Y. Tian, Improvement of Coral Sand With MICP Using Various Calcium Sources in Sea Water Environment, Frontiers in Physics 10 (2022) 82, https://doi.org/10.3389/FPHY.2022.825409/BIBTEX.
[38] C. Qian, R. Wang, L. Cheng, J. Wang, Theory of Microbial Carbonate Precipitation and Its Application in Restoration of Cement-based Materials Defects, Chinese Journal of Chemistry 28 (5) (2010) 847–857.
[39] M. Rahman, R.N. Hora, I. Ahenkorah, S. Beecham, R. Karim, A. Iqbal, State-of-the-art review of microbial-induced calcite precipitation and its sustainability in engineering applications, Sustainability 12 (15) (2020) 5281, https://doi.org/10.3390/su12156281.
[40] Raupach, M., & Wolff, L. (2009). Durability of adhesion of epoxy coatings on concrete; causes of delamination and blistering. Concrete Repair, Rehabilitation and Retrofitting II - Proceedings of the 2nd International Conference on Concrete Repair, Rehabilitation and Retrofitting, ICCRRR, 337–338. 10.1201/9781439828403.ch129.
[41] Y. Ryu, K.-E. Lee, I.-T. Cha, W. Park, Optimization of bacterial sporulation using economic nutrient for self-healing concrete, Journal of Microbiology 58 (4) (2020) 288–296.
[42] B.B.S. Singhal, R.P. Gupta, Applied Hydrogeology of Fractured Rocks, 2nd Ed., Springer, Netherlands, 2010, pp. 13–34.
[43] Snyder, K. A. (2003). Condition assessment of concrete nuclear structures considered for entombment. US Department of Commerce, Technology Administration, National Institute of Standards and Technology.
[44] C. Song, D. Elsworth, Y. Jia, J. Lin, Permeable rock matrix sealed with microbially-induced calcium carbonate precipitation: Evolutions of mechanical behaviors and associated microstructure, Engineering Geology 304 (2022) 106697.
[45] J.S. Thompson, D.E. Kissel, M.L. Cabrera, L.S. Sonon, Equilibration Reaction from Single Addition of Base to Determine Soil Lime Requirement, Soil Science Society of America Journal 74 (2) (2010) 663–669, https://doi.org/10.2136/sssaj2009.0168.
[46] D.J. Tobler, J.M. Minto, G. El Mountassir, R.J. Lunn, V.R. Phoenix, Microscale analysis of fractured rock sealed with microbially induced CaCO3 precipitation: influence on hydraulic and mechanical performance, Water Resources Research 54 (10) (2018) 8295–8308.
[47] Tziviloglou, E., Van Tittelboom, K., Palin, D., Wang, J., Sierra-Beltrán, M. G., Erşan, Y. Ç., ... & De Belie, N. (2016). Bio-based self-healing concrete: from research to field application. Self-healing materials, 345-385.
[48] K. Van Tittelboom, N. De Belie, W. De Muynck, W. Verstraete, Use of bacteria to repair cracks in concrete, Cement and Concrete Research 40 (1) (2010) 157–166, https://doi.org/10.1016/j.cemconres.2009.08.025.
[49] H. Wang, Life-cycle analysis of repair of concrete pavements, in: Eco-Efficient Repair and Rehabilitation of Concrete Infrastructures, Elsevier, 2018, pp. 723–738.
[50] J.Y. Wang, H. Soens, W. Verstraete, N. De Belie, Self-healing concrete by use of microencapsulated bacterial spores, Cement and concrete research 56 (2014) 139–152.
[51] V.S. Whiffin, L.A. Van Paassen, M.P. Harkes, Microbial carbonate precipitation as a soil improvement technique, Geomicrobiology Journal 24 (5) (2007) 417–423.
[52] D. Whiting, Permeability of selected concretes. Special, Publication 108 (1988) 195–222.
[53] V. Wiktor, H.M. Jonkers, Quantification of crack-healing in novel bacteria-based self-healing concrete, Cement and Concrete Composites 33 (7) (2011) 763–770, https://doi.org/10.1016/j.cemconcomp.2011.03.012.
[54] V. Wiktor, H.M. Jonkers, Bacteria-based concrete: From concept to market, Smart Materials and Structures 25 (8) (2016) 084006.
[55] C. Wu, J. Chu, S. Wu, L. Cheng, L.A. van Paassen, Microbially induced calcite precipitation along a circular flow channel under a constant flow condition, Acta Geotechnica 14 (3) (2019) 673–683.
[56] M.M.A. Helsel, C.F. Ferraris, M.D. Bentz, Comparative study of methods to measure the density of Cementious powders, Journal of testing and evaluation 44 (6) (2016).